SPE 93298

A Front-Tracking Method for Efficient Simulation of Miscible Gas Injection Processes

Ruben Juanes, SPE, Stanford U.; and **Knut–Andreas Lie**, SPE, SINTEF ICT

This paper was prepared for presentation at the 2005 SPE Reservoir Simulation Symposium held in Houston, Texas U.S.A., 31 January 2005–2 February 2005.

Abstract

This paper presents a front-tracking method for the numerical simulation of first-contact miscible gas injection processes. The method is developed for constructing very accurate (or even exact) solutions to one-dimensional initial-boundary-value problems in the form of a set of evolving discontinuities. The evolution of the discontinuities is given by analytical solutions to Riemann problems. A complete analytical Riemann solver is presented along with methods for simplifying the wave structure for Riemann problems of small amplitude. Several representative examples are used to illustrate the excellent behavior of the front-tracking method.

The front-tracking method can be extended to simulate higher-dimensional processes through the use of streamlines. The paper presents an application of this computational framework for the simulation of miscible flooding in a three-dimensional, highly heterogeneous formation, and demonstrate that a miscible water-alternating-gas injection scheme is more efficient than waterflooding or gas injection alone.

Introduction

Gas injection is one of the most widely used enhanced oil recovery processes.[1–3] The fundamental principle is the development of miscibility between the resident oil phase and the injected gas, in order to enhance the mobility of the hydrocarbon phase and to achieve a high displacement efficiency. In general, miscibility between the oil present in the reservoir and the injected gas leads to a complex set of interactions described by thermodynamical equilibrium of the system, in which components of the gas dissolve in the oil, and components of the oil transfer to the vapor.[4–6]

In this paper, we restrict our attention to simplified thermodynamical systems that can be approximated by *first-contact miscible* phase behavior. The underlying assumption is that the injection gas (solvent) and the resident oil mix in all proportions to form a single hydrocarbon phase. This scenario is optimal with respect to local displacement efficiency, and can be achieved in practice if the gas is injected at a pressure above the minimum miscibility pressure.[7,8]

We present a computational framework for the efficient simulation of first-contact miscible processes in three-dimensional, heterogeneous reservoir models. The key ingredients of our approach are:

1. An analytical solution of the one-dimensional Riemann problem for a three-component, two-phase system under the assumption of first-contact miscibility of the hydrocarbon components.

2. A front-tracking algorithm that makes use of the analytical Riemann solver as a building block for obtaining approximate solutions to general one-dimensional problems.

3. A streamline simulator that decouples the three-dimensional transport equations into a set of one-dimensional problems along streamlines.

The proposed framework was introduced by the authors for the simulation of immiscible three-phase flow,[9,10] and is extended here to miscible gas injection problems.

The Riemann problem consists in solving a system of conservation laws in an infinite one-dimensional domain, with piecewise constant initial data separated by a single discontinuity. The development of analytical solutions to the Riemann problem of multiphase, multicomponent flow has received considerable attention over the past two decades (see, e.g.[3] and the references therein). Riemann

solutions have been constructed for two-phase and three-phase systems with complex phase behavior for particular initial and injection conditions. However, the development of complete Riemann solvers is a much more challenging task. A Riemann solver is a mathematical algorithm that provides the solution to the Riemann problem for *any* initial and injection states. A Riemann solver for polymer flooding was originally presented by Isaacson,[11] and then extended by Johansen and Winther to account for adsorption in two-component[12] and multicomponent systems.[13,14] The principle behind polymer flooding is the addition of a *water-soluble* polymer to the injected water to *increase* its viscosity and, consequently, the efficiency of a waterflood. We are interested in miscible flooding, where the injected solvent readily mixes with the *oil* in place, and *reduces* the viscosity of the hydrocarbon phase. However, under a proper change of variables, the mathematical structure of the equations is virtually identical to that of polymer flooding. Therefore, we rely heavily on the developments of Isaacson[11] and Johansen and Winther[12] when formulating the complete Riemann solver for first-contact miscible flooding. We extend the formulation (slightly) by accounting for the presence of connate water and residual oil. We also pay special attention to the efficient implementation of the analytical solver, because typical applications require the evaluation of hundreds of millions of Riemann problems.

Front-tracking methods refer to numerical schemes that perform tracking of shocks and other evolving discontinuities.[15] They were developed to construct approximate and exact solutions to hyperbolic systems of conservation laws in one space dimension with general initial data,[16] and they have been used as an essential tool in proving uniqueness of the solution.[17] Early application areas of the method include gas dynamics[18] and reservoir simulation.[19] Of particular interest is the work of Risebro and Tveito,[20] where the front-tracking method is applied to the multicomponent polymer flooding system in one dimension. In our implementation of the front-tracking method, all waves are treated as discontinuities. Shock waves and contact discontinuities are tracked exactly, and rarefaction waves are approximated by small inadmissible shocks. The discontinuities are tracked until they interact and define a new Riemann problem. The approximate solution of this new Riemann problem leads to a new set of discontinuities that need to be tracked. Repeated application of this procedure allows marching in time. The main advantages of the front-tracking method just described are: (1) it captures discontinuities exactly without introducing any numerical diffusion; (2) it is grid-independent; (3) it is unconditionally stable; and (4) it can be extremely efficient if an analytical Riemann solver is available.

In this paper, we propose the use of streamlines to perform numerical simulation of miscible flooding in higher-dimensional, heterogeneous media. Streamline methods are based on a staggered solution of a global pressure equation and the system of transport equations.[21] Solution of the pressure equation defines the velocity field used to trace the streamlines. In this way, streamline methods decouple the three-dimensional equations describing the transport of individual components into a set of one-dimensional problems along streamlines. With a proper parameterization of the streamlines, the numerical solution is then obtained using the front-tracking method described above. Therefore, the method is fundamentally different from that of Haugse et al.,[22] where front-tracking is applied in conjunction with operator-splitting, and one-dimensional problems are solved sequentially in each spatial dimension.

An outline of the paper is as follows. We first derive the mathematical model describing the first-contact miscible system, and introduce the conservation variables employed in characterizing the solution. We comment on the mathematical character of the system of equations, highlighting the fact that it is not strictly hyperbolic. In Section 3 we describe the different waves that may be present, and the complete solution to the Riemann problem. The front-tracking algorithm is given and discussed in Section 4. In Section 5 we present several representative one-dimensional simulations that illustrate the excellent behavior of the front-tracking method. In Section 6, we present an application of the proposed computational framework to the simulation of miscible flooding in a three-dimensional, highly heterogeneous formation. We compare recovery predictions for different injection scenarios, and conclude that a miscible water-alternating-gas (WAG) injection scheme is more effective than waterflooding or gas injection alone. In Section 7 we gather the main conclusions and anticipate ongoing and future work.

Mathematical model

Governing equations. We derive briefly the governing equations for one-dimensional, two-phase, three-component flow in porous media. The three components are referred to as water (w), oil (o) and solvent or gas (g). In what follows, we shall assume that water is immiscible, and forms an aqueous phase (w). We shall also assume that the two hydrocarbon components (oil and solvent) are fully miscible, and form a nonaqueous hydrocarbon phase (h).

The one-dimensional conservation for each of the components can be written as:

$$\frac{\partial m_i}{\partial t} + \frac{\partial F_i}{\partial x} = 0, \qquad i = w, o, g. \tag{1}$$

where m_i is the mass of component i per unit volume of porous medium, and F_i is the mass flux of that component. The mass densities are expressed in the following form:

$$m_w = \rho_w \phi S_w, \tag{2}$$

$$m_o = \rho_h \phi S_h \chi_o, \tag{3}$$

$$m_g = \rho_h \phi S_h \chi_g, \tag{4}$$

where ρ_α ($\alpha = w, h$) are the densities of each phase, ϕ is the porosity, S_α are the saturations (volume fractions of each phase), and χ_j ($j = o, g$) are the mass fractions of oil and solvent in the hydrocarbon phase. Equations (2)–(4) are subject to the following constraints:

$$S_w + S_h \equiv 1, \tag{5}$$

$$\chi_o + \chi_g \equiv 1. \tag{6}$$

The mass flux of each component is given by:

$$F_w = \rho_w \phi v_w, \tag{7}$$
$$F_o = \chi_o \rho_h \phi v_h, \tag{8}$$
$$F_g = \chi_g \rho_h \phi v_h, \tag{9}$$

where v_α are the average velocities of each phase. A constitutive model for the phase velocities is given by the multiphase extension of Darcy's law. Neglecting the effect of gravity and capillary forces, they take the form:

$$v_w = -\frac{k}{\phi}\frac{k_{rw}}{\mu_w}\nabla p, \tag{10}$$
$$v_h = -\frac{k}{\phi}\frac{k_{rh}}{\mu_h}\nabla p, \tag{11}$$

where k is the absolute permeability of the medium, p is the pressure, and $k_{r\alpha}$ and μ_α are the relative permeability and the dynamic viscosity of the α-phase, respectively. For the purpose of this paper, we shall assume that relative permeabilities are functions of the phase saturation only.

Using Equations (2)–(9) in Equation (1), and assuming incompressible fluids which do not experience volume change in mixing (ρ_α = const) and rigid medium (ϕ = const), the mass conservation equations for all three components are written as:

$$\frac{\partial S_w}{\partial t} + \frac{\partial v_w}{\partial x} = 0, \tag{12}$$
$$\frac{\partial((1-S_w)(1-\chi_g))}{\partial t} + \frac{\partial((1-\chi_g)v_h)}{\partial x} = 0, \tag{13}$$
$$\frac{\partial((1-S_w)\chi_g)}{\partial t} + \frac{\partial(\chi_g v_h)}{\partial x} = 0. \tag{14}$$

Summing Equations (12)–(14), we obtain the *pressure equation*:

$$\frac{\partial v_T}{\partial x} = 0, \tag{15}$$

where $v_T := v_w + v_h$ is the total velocity. The pressure equation is an elliptic equation, which dictates that the total velocity is at most a function of time. We introduce the fractional flow functions:

$$f_w := \frac{\lambda_w}{\lambda_T}, \tag{16}$$
$$f_h := \frac{\lambda_h}{\lambda_T}, \tag{17}$$

where $\lambda_\alpha = k_{r\alpha}/\mu_\alpha$ is the relative mobility of the α-phase, and $\lambda_T := \lambda_w + \lambda_h$ is the total mobility. With these definitions, a set of two independent conservation equations is:

$$\frac{\partial S_w}{\partial t} + v_T \frac{\partial f_w}{\partial x} = 0, \tag{18}$$
$$\frac{\partial((1-S_w)\chi_g)}{\partial t} + v_T \frac{\partial((1-f_w)\chi_g)}{\partial x} = 0. \tag{19}$$

It proves useful to express the governing equations above in terms of the following *conservation variables:*

$$S \equiv S_w \ : \quad \text{water saturation}, \tag{20}$$
$$C \equiv (1-S_w)\chi_g \ : \quad \text{solvent concentration}. \tag{21}$$

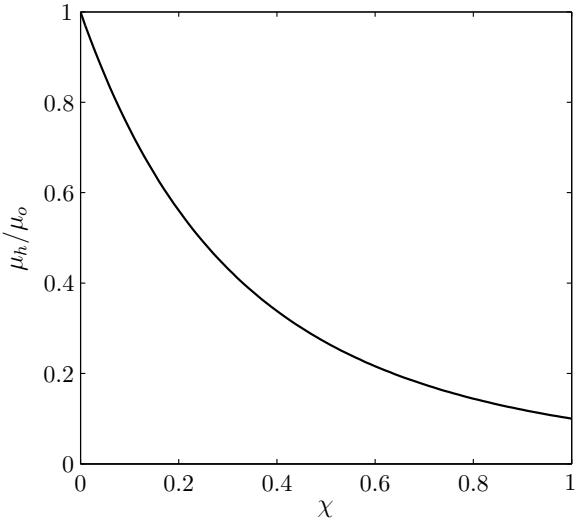

Fig. 1— Typical dependence of the hydrocarbon viscosity on the solvent mass fraction.

In what follows, we drop the subscript from the solvent mass fraction, $\chi \equiv \chi_g$. After proper re-scaling of the time variable to eliminate the total velocity and letting f denote the water fractional flow function, the final form of the conservation equations is:

$$\frac{\partial S}{\partial t} + \frac{\partial f}{\partial x} = 0, \tag{22}$$
$$\frac{\partial C}{\partial t} + \frac{\partial}{\partial x}\left(\frac{1-f}{1-S}C\right) = 0. \tag{23}$$

To close the mathematical model, we must provide constitutive relations for the hydrocarbon viscosity and the relative permeabilities. The viscosity of the hydrocarbon phase depends on the viscosities of the oil and gas components μ_o and μ_g (taken as constants) and the gas mass fraction χ in the hydrocarbon phase. Since the gas viscosity is lower (usually much lower) than the oil viscosity, the hydrocarbon viscosity is a decreasing function of the gas mass fraction (see **Fig. 1**).

We assume that the hydrocarbon relative permeability does not depend on the amount of solvent. In particular, this means that the residual hydrocarbon saturation is invariant. Thus, relative permeabilities of the aqueous and hydrocarbon phases are functions of the water saturation only. Typical behavior of these functions is shown in **Fig. 2**, where we account for the presence of connate water and residual oil. As a result, the fractional flow is a function of both water saturation and solvent concentration:

$$f = \frac{\frac{k_{rw}(S)}{\mu_w}}{\frac{k_{rw}(S)}{\mu_w} + \frac{k_{rh}(S)}{\mu_h(\chi)}} = f(S,C). \tag{24}$$

Since the hydrocarbon viscosity decreases with the solvent fraction, the overall mobility of the hydrocarbon phase is enhanced, resulting in lower values of the water fractional flow. The dependence of the fractional flow function on the solvent mass fraction is illustrated in **Fig. 2**.

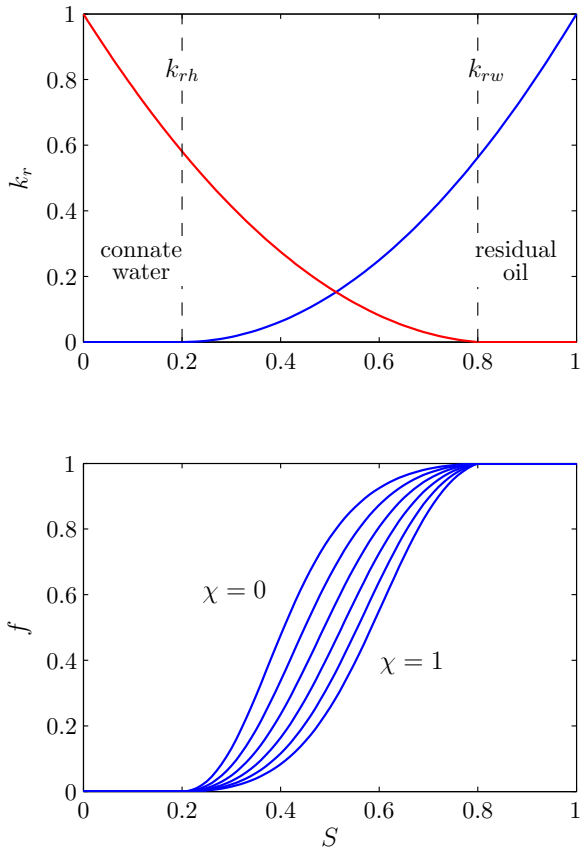

Fig. 2— Top: relative permeabilities of the water and hydrocarbon phases. Bottom: dependence of the fractional flow function on the solvent mass fraction.

Mathematical character of the equations. We express the system of conservation laws (22)–(23) in vector form:

$$\partial_t \begin{bmatrix} S \\ C \end{bmatrix} + \partial_x \begin{bmatrix} f \\ \frac{1-f}{1-S} C \end{bmatrix} = \begin{bmatrix} 0 \\ 0 \end{bmatrix}. \tag{25}$$

The solution vector (S, C) is restricted to lie on the unit triangle:

$$\mathcal{U} \equiv \{(S,C) : S \geq 0,\ C \geq 0,\ S + C \leq 1\}. \tag{26}$$

For smooth solutions, the system (25) can be written as

$$\partial_t \begin{bmatrix} S \\ C \end{bmatrix} + A(S,C) \partial_x \begin{bmatrix} S \\ C \end{bmatrix} = \begin{bmatrix} 0 \\ 0 \end{bmatrix}. \tag{27}$$

where A is the Jacobian matrix of the system:

$$A(S,C) := \begin{bmatrix} \frac{\partial f}{\partial S} & \frac{\partial f}{\partial C} \\ \left(\frac{1-f}{1-S} - \frac{\partial f}{\partial S}\right) \frac{C}{1-S} & \frac{1-f}{1-S} - \frac{\partial f}{\partial C} \frac{C}{1-S} \end{bmatrix}. \tag{28}$$

The local character of the system is determined by the eigenvalues and eigenvectors of the Jacobian matrix.[23] The eigenvalues are given by:

$$\begin{aligned} \nu_s = \nu_s(S,C) &= \frac{\partial f}{\partial S} - \frac{\partial f}{\partial C} \frac{C}{1-S}, \\ \nu_c = \nu_c(S,C) &= \frac{1-f}{1-S}, \end{aligned} \tag{29}$$

and the corresponding eigenvectors are:

$$\begin{aligned} r_s &= \begin{bmatrix} 1 \\ -\frac{C}{1-S} \end{bmatrix}, \\ r_c &= \begin{bmatrix} \frac{\partial f}{\partial C} \\ \frac{1-f}{1-S} - \frac{\partial f}{\partial S} \end{bmatrix}. \end{aligned} \tag{30}$$

The eigenvalues ν_s and ν_c (when they are real) are the characteristic speeds of propagation of waves of the S- and C-family, respectively. The system is hyperbolic if the eigenvalues are real, and strictly hyperbolic if the eigenvalues are real and distinct. In the latter case, the matrix is diagonalizable and there exist two real and linearly independent eigenvectors. If the two eigenvalues are complex conjugates, the system is said to be elliptic.

It is easy to show that the system (25) is hyperbolic, but not everywhere strictly hyperbolic. Loss of strict hyperbolicity occurs at two regions of the composition triangle. First, in the region of residual oil, both eigenvalues are identically equal to zero. The Jacobian matrix is the zero matrix, and every direction is characteristic. Second, there is a curve in phase space at which the eigenvalues coincide, $\nu_s = \nu_c$. This curve divides the unit triangle $\mathcal{U}$ into two regions:

$$\begin{aligned} \mathcal{L} &\equiv \{(S,C) : \nu_s < \nu_c\}, \\ \mathcal{R} &\equiv \{(S,C) : \nu_s > \nu_c\}. \end{aligned} \tag{31}$$

We denote this curve as the *transition curve* $\mathcal{T}$ because the two families of eigenvalues change order as $\mathcal{T}$ is crossed. Since the fractional flow function is monotonic with respect to the solvent mass fraction χ, the transition curve intersects each line $\chi = \text{const}$ at exactly one point.

For the first-contact miscible model considered in this paper, the Jacobian matrix is not diagonalizable on $\mathcal{T}$, that is, A has only one independent eigenvector:

$$r_s\big|_{\mathcal{T}} = r_c\big|_{\mathcal{T}} = \begin{bmatrix} 1 \\ -\frac{C}{1-S} \end{bmatrix}. \tag{32}$$

The system is said to have a parabolic degeneracy on $\mathcal{T}$. This behavior is qualitatively very different from that of a model that assumes constant hydrocarbon viscosity. In such model, because the fractional flow f is a function of S only, the system is a multiple of the identity along the transition curve, and every direction is characteristic.

The Riemann problem

The Riemann problem consists in finding the weak solution to the system of hyperbolic conservation laws:

$$\partial_t u + \partial_x f = 0, \quad -\infty < x < \infty, \quad t > 0, \tag{33}$$

with the following initial conditions:

$$u(x,0) = \begin{cases} u_l & \text{if } x < 0, \\ u_r & \text{if } x \geq 0. \end{cases} \tag{34}$$

The state $u_l = (S_l, C_l)$ is the 'left' or 'injected' state, and $u_r = (S_r, C_r)$ is the 'right' or 'initial' state. The system of equations (33) and the initial condition (34) are invariant

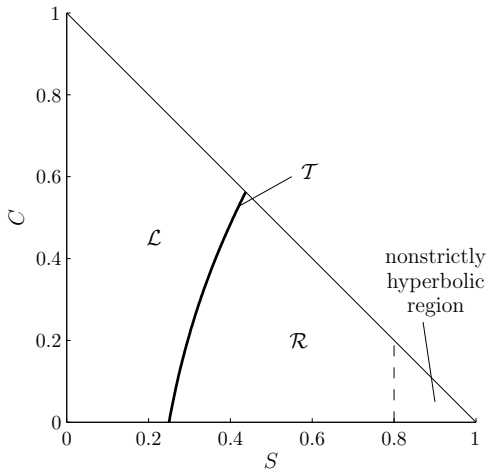

Fig. 3— Transition curve $\mathcal{T}$ ($\nu_s = \nu_c$) and the regions $\mathcal{L}$ ($\nu_s < \nu_c$) and $\mathcal{R}$ ($\nu_s > \nu_c$) on the ternary diagram.

under uniform stretching of coordinates $(x,t) \mapsto (cx, ct)$. The solution must consist of centered waves emanating from the origin $(x,t) = (0,0)$. Therefore, we seek a self-similar solution

$$u(x,t) = U(\zeta), \tag{35}$$

where the similarity variable is $\zeta = x/t$.

Wave types. In this section we describe the types of centered waves that arise in the solution of the Riemann problem of miscible three-component flow.

Integral curves. If the solution $U(\zeta)$ is smooth, it must satisfy

$$A(U)U' = \zeta U', \tag{36}$$

that is, ζ is an eigenvalue and U' is the corresponding eigenvector. Therefore, smooth waves (rarefactions) must lie on an integral curve of the right eigenvectors. States U along an integral curve are defined by the differential equation

$$\frac{\mathrm{d}U}{\mathrm{d}\tau} = r_i(U(\tau)), \quad i = s, c. \tag{37}$$

Performing the integration analytically, the two families of integral curves are given by the equations:

$$\begin{aligned} S\text{-family}: &\quad \frac{C}{1-S} = \text{const}, \\ C\text{-family}: &\quad \nu_c = \text{const}. \end{aligned} \tag{38}$$

In the context of compositional displacements, integral curves of the S-family are known as *tie-line* paths, and curves of the C-family are termed *nontie-line paths*.[3] The integral curves of the system of interest are shown in **Fig. 4**.

Discontinuous solutions must satisfy an integral version of the mass conservation equations, known as the Rankine–Hugoniot conditions. The set of states U that can be joined to a reference state u_l by a discontinuity satisfy:

$$f(u_r) - f(u_l) = \sigma\ (u_r - u_l), \tag{39}$$

where σ is the speed of propagation of the discontinuity. For the flux vector f of the first-contact miscible problem,

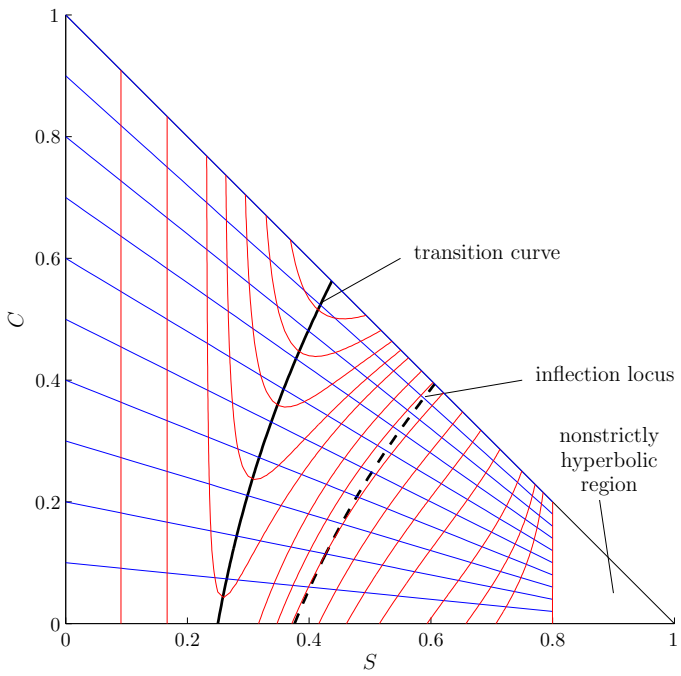

Fig. 4— Integral curves of the S-family (blue) and C-family (red) on the ternary diagram. Also shown are the transition curve, where eigenvalues of different families coincide, and the inflection locus of the S-family.

Equation (39) admits two families of solutions, which define the Hugoniot locus of the S- and C-family. In general, integral curves and Hugoniot loci do not coincide, but they have second order tangency (same slope and curvature) at any given state, so they are locally very similar.

The integral curves of the miscible system have the following special features: (1) integral curves of the S-family are straight lines, which means that they they have zero curvature; (2) the eigenvalue ν_c is constant along integral curves of the C-family, which means that these curves correspond to contact discontinuities. The immediate consequence of these properties is that, for the solvent system, Hugoniot loci and integral curves *coincide*.

Waves of the S-family (Tie-line waves). Waves of the S-family are solutions of the classical Buckley–Leverett equation. The wave curves are straight lines on composition space, corresponding to lines of constant solvent mass fraction

$$\chi = \text{const}. \tag{40}$$

The characteristic velocity ν_s is not constant along integral curves of the S-family. Let us define

$$V_s(u) := \nabla \nu_s(u) \cdot r_s(u). \tag{41}$$

Since the convexity function V_s changes sign, the S-field is a nongenuinely nonlinear field in the sense of Lax.[24] The *inflection locus* is the set of states where $V_s = 0$, which separates regions of different convexity (see **Fig. 4**). In our model, the fractional flow function is S-shaped, so the inflection locus intersects each tie-line at exactly one point, which corresponds to a *maximum* of the eigenvalue ν_s. It can be shown that, under these conditions, a S-wave can

only be of three types: rarefaction, shock, and rarefaction-shock.[25] The admissibility of a S-wave is based on the e-Lax entropy condition (convex-hull construction).[26,27] A robust and efficient algorithm for the determination of the wave structure in the Buckley–Leverett problem is presented elsewhere.[28]

Waves of the C-family (Nontie-line waves). The characteristic speed ν_c is constant along wave curves of the C-family. The C-field is a linearly degenerate field in the sense of Lax,[24] and the waves of this family are contact discontinuities. The immediate computational benefit of this property is that evaluation of nontie-line paths does not require numerical integration of an ordinary differential equation: the C-waves are completely determined by the algebraic relation

$$\nu_c = \text{const.} \tag{42}$$

Application of the e-Lax entropy condition[27] precludes the possibility that a C-wave joins constant states on opposite sides of the transition curve.[11]

Admissible wave sequences. In general, the solution to the Riemann problem consists of a sequence of the centered waves described in the previous section. For 2×2 strictly hyperbolic systems, whose fields satisfy certain nondegeneracy conditions, the solution will comprise at most two waves, which are strictly separated:[27]

$$u_l \xrightarrow{\mathcal{W}_1} u_m \xrightarrow{\mathcal{W}_2} u_r \tag{43}$$

For nonstrictly hyperbolic systems, however, the solution may involve more than two waves. In addition to the slow and fast waves characteristic of a strictly hyperbolic system, *transitional waves* may be necessary in the construction of a solution.[29,30] The system describing miscible flooding is a good example of this behavior.

Before describing the complete solution, we give the admissible pairs of waves that may be present.

The case $u_l \xrightarrow{\mathcal{C}} u_m \xrightarrow{\mathcal{S}} u_r$. Adapting the analysis of Isaacson[11] to our model problem, it can be shown that the sequence of waves $u_l \xrightarrow{\mathcal{C}} u_m \xrightarrow{\mathcal{S}} u_r$, that is, the combination of a slower C-wave with a faster S-wave, is admissible only in the following three cases:

(a) If $u_m \in \mathcal{T}$ and $u_r \in \mathcal{R}$.

(b) If $u_m \in \mathcal{R}$ and $u_r \in \mathcal{R}$.

(c) If $u_m \in \mathcal{R}$ and $u_r \in \mathcal{L}$ such that $\nu_c(u_r) \geq \nu_c(u_m)$.

Examples of each of these wave sequences are given in **Fig. 5**. The top row of figures show admissible sequences of wave curves in composition space. The bottom row of figures show the fractional flow curve corresponding to the tie-line passing through the intermediate state u_m. In all three cases, the characteristic speed of the C-wave (slope of the red line) is less than the characteristic speed of the S-wave (slope of the blue line), indicating admissibility of the wave sequence.

The case $u_l \xrightarrow{\mathcal{S}} u_m \xrightarrow{\mathcal{C}} u_r$. Similarly, it can be shown that the sequence of waves $u_l \xrightarrow{\mathcal{S}} u_m \xrightarrow{\mathcal{C}} u_r$, that is, the combination of a slower S-wave with a faster C-wave, is admissible only in the following three cases:

(a) If $u_m \in \mathcal{T}$ and $u_l \in \mathcal{L}$.

(b) If $u_m \in \mathcal{L}$ and $u_l \in \mathcal{L}$.

(c) If $u_m \in \mathcal{L}$ and $u_l \in \mathcal{R}$ such that $\nu_c(u_l) \geq \nu_c(u_m)$.

In **Fig. 6** we show examples of each of these wave pairs, illustrating the sequence of wave curves on the composition diagram and the fractional flow curve of the tie-line passing through u_m.

Solution of the Riemann problem. The global solution of the Riemann problem is obtained by joining waves that form a compatible sequence. Motivated by the admissible wave structure of Cases 1 and 2 above, and following Isaacson,[11] we define several regions in the composition diagram that will allow a straightforward characterization of the wave structure of the solution.

- The case $u_l \in \mathcal{L}$ (**Fig. 7**(a)): One must first identify the tie-line $\chi = \chi(u_l)$ associated with the left state, and the intersection u_t of this tie-line and the transition curve $\mathcal{T}$. Then, we define the following three nonoverlapping regions that cover the entire ternary diagram $\mathcal{U}$:
  1. Region $\mathcal{L}_1$: It contains the set of states u satisfying that $\nu_s(u) < \nu_c(u)$ and $\nu_c(u) < \nu_c(u_t)$. Therefore, it is bounded from the right by the transition curve $\mathcal{T}$ and the left branch of the nontie-line passing through the intersection point u_t.
  2. Region $\mathcal{L}_2$: It contains the set of states u satisfying that $\nu_s(u) > \nu_c(u_t)$ and $\chi(u) > \chi(u_t)$. It is bounded from the left by the left branch of the nontie-line passing through u_t and from below by the tie-line passing through u_t.
  3. Region $\mathcal{L}_3$: It contains the set of states u satisfying that $\nu_s(u) > \nu_c(u)$ and $\chi(u) < \chi(u_t)$. It is bounded from the left by the transition curve $\mathcal{T}$ and from above by the tie-line passing through u_t.
- The case $u_l \in \mathcal{R}$ (**Fig. 7**(b)): We first find the nontie-line $\nu_c = \nu_c(u_l)$ associated with the left state, and the intersection u_t of this nontie-line and the transition curve $\mathcal{T}$. It is important to note that this intersection point may be outside the ternary diagram. In that case, some of the regions defined below will be empty:
  1. Region $\mathcal{R}_1$: It contains the set of states u satisfying that $\nu_s(u) < \nu_c(u)$ and $\nu_c(u) < \nu_c(u_t)$. If the intersection point u_t is inside the ternary diagram, this region is bounded from the right by the transition curve $\mathcal{T}$ and the left branch of the nontie-line passing through the intersection point u_t. Otherwise, it is bounded from the right entirely by the left branch of the nontie-line, and it is empty if $\nu_c(u_l) < 1$.

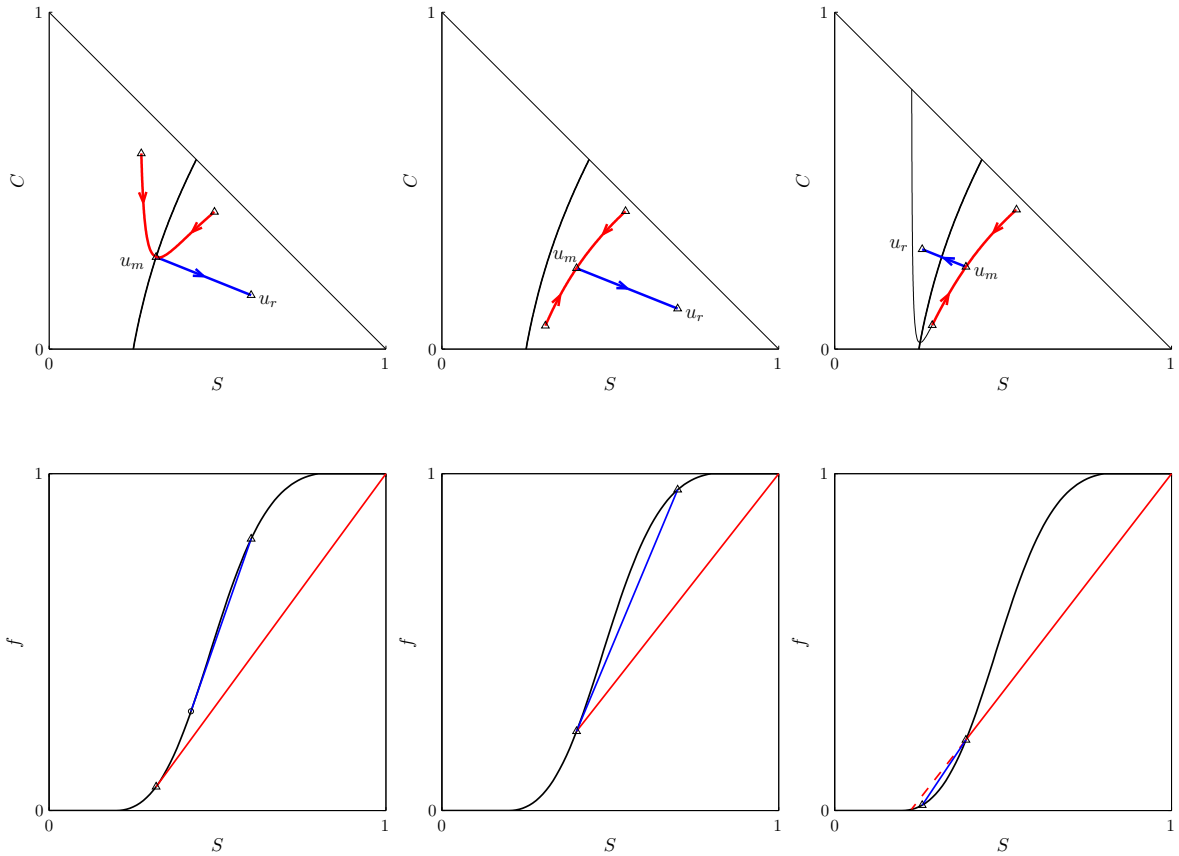

(a) $u_m \in \mathcal{T}$, $u_r \in \mathcal{R}$ (b) $u_m \in \mathcal{R}$, $u_r \in \mathcal{R}$ (c) $u_m \in \mathcal{R}$, $u_r \in \mathcal{L}$

Fig. 5— All three types of compatible wave sequences of type $u_l \xrightarrow{\mathcal{C}} u_m \xrightarrow{\mathcal{S}} u_r$.

2. Region $\mathcal{R}_2$: It contains the set of states u satisfying that $\nu_s(u) > \nu_c(u_t)$ and $\chi(u) > \chi(u_t)$. If the intersection point u_t is inside the ternary diagram, this region is bounded from the left by the left branch of the nontie-line passing through u_t and from below by the tie-line passing through u_t. If u_t is outside the composition triangle, this region is only bounded from the left by the left branch of the nontie-line $\nu_c = \nu_c(u_l)$. If $\nu_c(u_l) < 1$, this region covers the entire triangle.
3. Region $\mathcal{R}_3$: It contains the set of states u satisfying that $\nu_s(u) > \nu_c(u)$ and $\chi(u) < \chi(u_t)$. If the intersection point u_t is inside the ternary diagram, this region is bounded from the left by the transition curve $\mathcal{T}$ and from above by the tie-line passing through u_t; otherwise it is empty.

We are now in position to give the global structure of the solution to the Riemann problem.[11]

- The case $u_l \in \mathcal{L}$ (**Fig. 8**): If the left state u_l belongs to the region $\mathcal{L}$, that is, if $\nu_s(u_l) < \nu_c(u_l)$, the global solution to the Riemann problem is of one of the following types:
  1. $u_r \in \mathcal{L}_1$ (**Fig. 8**(a)): $u_l \xrightarrow{\mathcal{S}} u_m \xrightarrow{\mathcal{C}} u_r$.
  2. $u_r \in \mathcal{L}_2$ (**Fig. 8**(b)): $u_l \xrightarrow{\mathcal{S}} u_m^{(1)} \xrightarrow{\mathcal{C}} u_m^{(2)} \xrightarrow{\mathcal{S}} u_r$.
  3. $u_r \in \mathcal{L}_3$ (**Fig. 8**(c)): $u_l \xrightarrow{\mathcal{S}} u_m^{(1)} \xrightarrow{\mathcal{C}} u_m^{(2)} \xrightarrow{\mathcal{S}} u_r$.
- The case $u_l \in \mathcal{R}$ (**Fig. 9**): If the left state u_l belongs to the region $\mathcal{R}$, that is, if $\nu_s(u_l) > \nu_c(u_l)$, the global solution to the Riemann problem is of one of the following types:
  1. $u_r \in \mathcal{R}_1$ (**Fig. 9**(a)): $u_l \xrightarrow{\mathcal{S}} u_m \xrightarrow{\mathcal{C}} u_r$.
  2. $u_r \in \mathcal{R}_2$ (**Fig. 9**(b)): $u_l \xrightarrow{\mathcal{C}} u_m \xrightarrow{\mathcal{S}} u_r$.
  3. $u_r \in \mathcal{R}_3$ (**Fig. 9**(c)): $u_l \xrightarrow{\mathcal{S}} u_m^{(1)} \xrightarrow{\mathcal{C}} u_m^{(2)} \xrightarrow{\mathcal{S}} u_r$.

Remarks.

1. Of course, the solution may involve a single wave if the left and right states are on the same tie-line ($u_l \xrightarrow{\mathcal{S}} u_r$) or on the same nontie-line path ($u_l \xrightarrow{\mathcal{C}} u_r$).
2. Several of the solutions are composed of three waves. In all these cases, the transitional wave is a contact discontinuity.

Convergence of finite difference solutions. The purpose of this section is to illustrate the difficulty of standard numerical methods in producing accurate solutions to the Riemann problem. The slow convergence of finite difference solutions to the analytical solution of nonstrictly hyperbolic conservation laws has been noted by many authors.[12,20,31] The main reason is the presence of contact

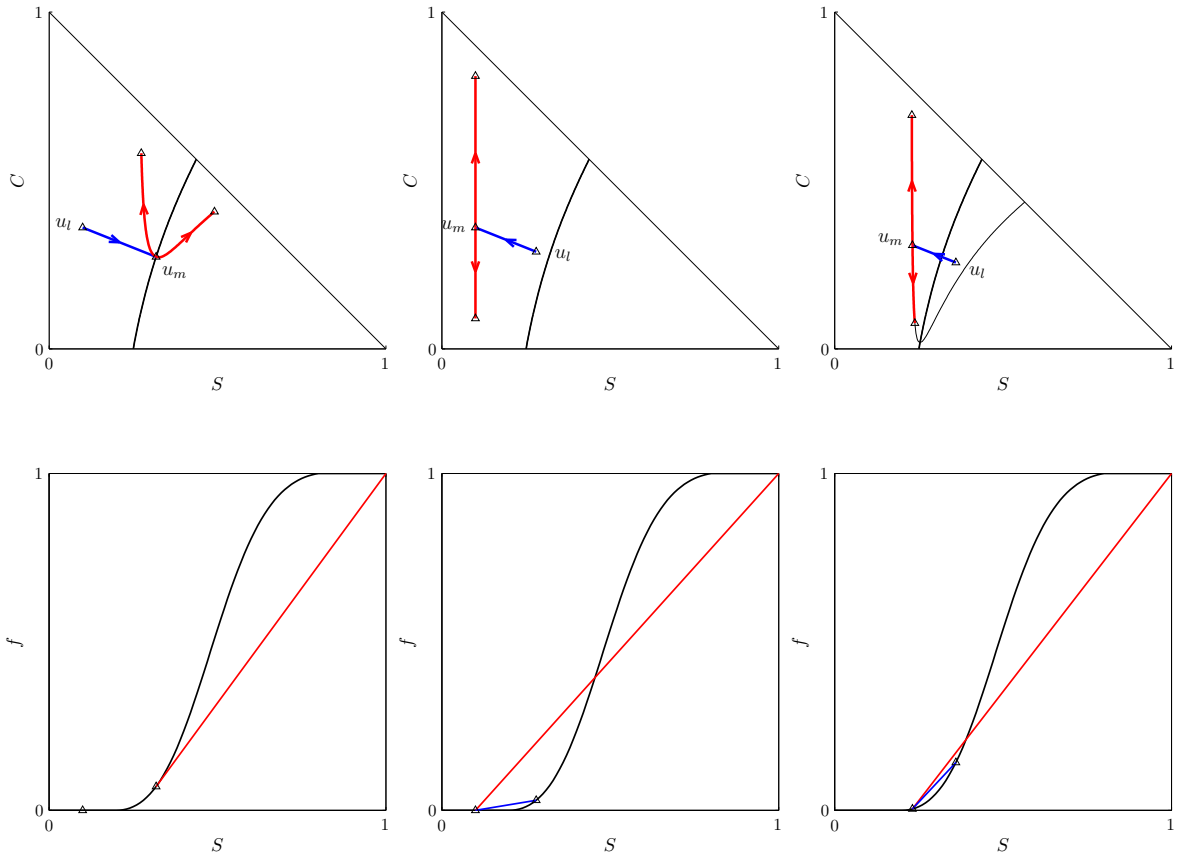

(a) $u_m \in \mathcal{T}$, $u_r \in \mathcal{R}$ (b) $u_m \in \mathcal{L}$, $u_r \in \mathcal{L}$ (c) $u_m \in \mathcal{L}$, $u_r \in \mathcal{R}$

Fig. 6— All three types of compatible wave sequences of type $u_l \xrightarrow{\mathcal{S}} u_m \xrightarrow{\mathcal{C}} u_r$.

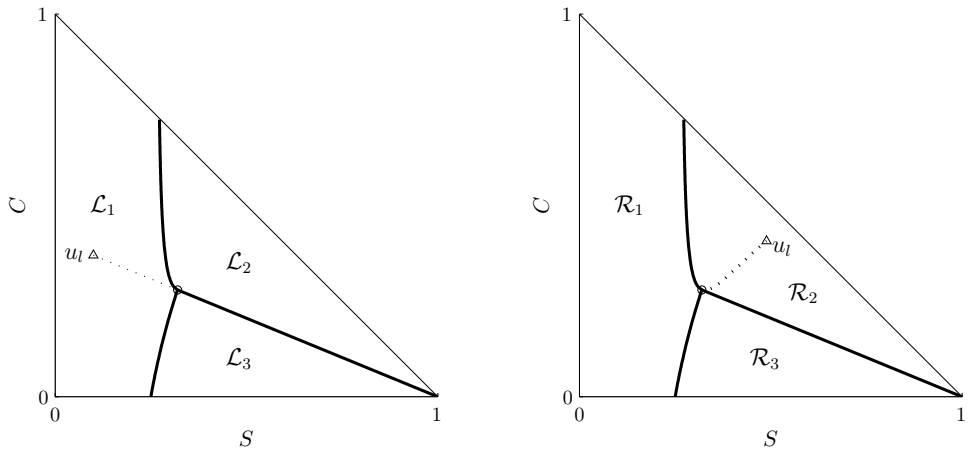

(a) $u_l \in \mathcal{L}$ (b) $u_l \in \mathcal{R}$

Fig. 7— Regions on the ternary diagram defining the global wave structure of the Riemann solution.

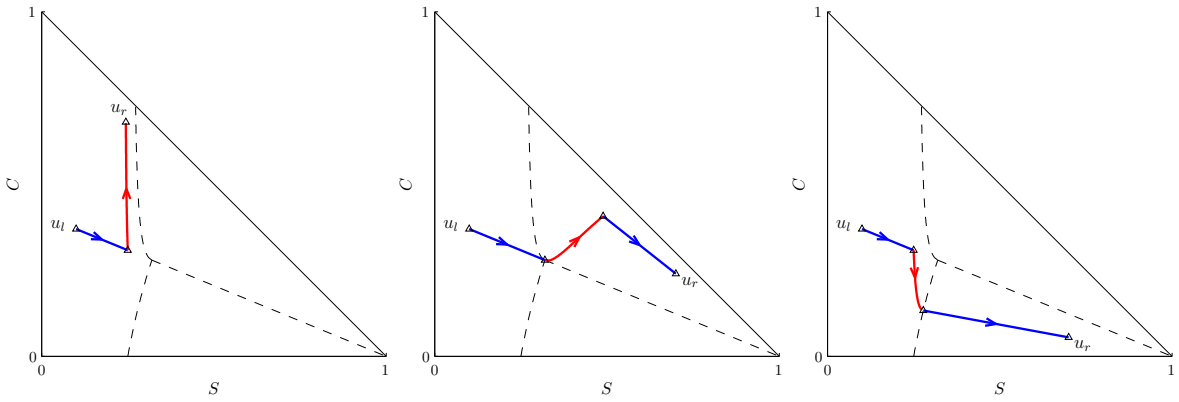

(a) $u_l \in \mathcal{L}$, $u_r \in \mathcal{L}_1$ (b) $u_l \in \mathcal{L}$, $u_r \in \mathcal{L}_2$ (c) $u_l \in \mathcal{L}$, $u_r \in \mathcal{L}_3$

Fig. 8— Wave structure of the solution when $u_l \in \mathcal{L}$.

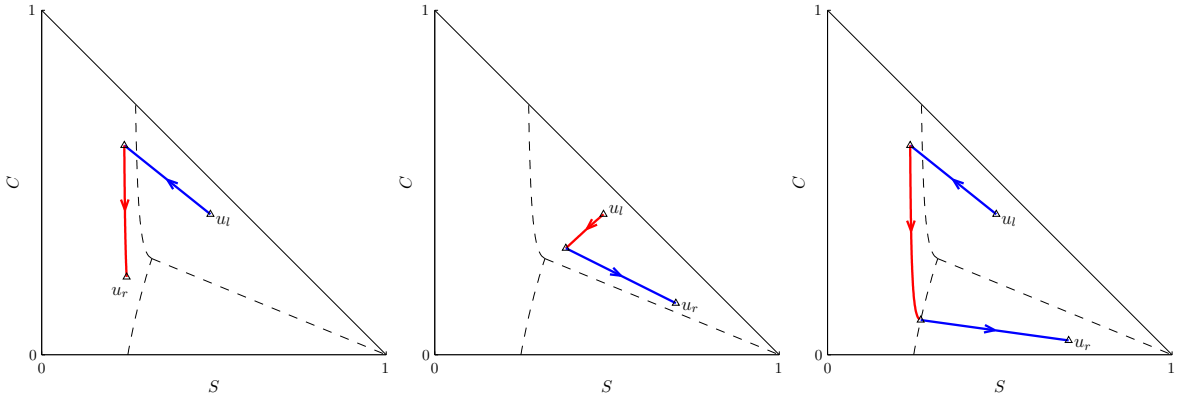

(a) $u_l \in \mathcal{R}$, $u_r \in \mathcal{R}_1$ (b) $u_l \in \mathcal{R}$, $u_r \in \mathcal{R}_2$ (c) $u_l \in \mathcal{R}$, $u_r \in \mathcal{R}_3$

Fig. 9— Wave structure of the solution when $u_l \in \mathcal{R}$.

discontinuities in the solution. Contact discontinuities are indifferent waves and, unlike genuine shocks, are *not* self-sharpening. As a result, some essential features of the solution may be overwhelmed by numerical diffusion introduced by standard finite difference schemes.

In **Fig. 10** we compare the analytical solution to a Riemann problem of type $\mathcal{R}_3$ with finite difference solutions on increasingly refined grids. We used the single-point upstream finite difference method, and a Crank-Nicolson scheme for integration in time. The time step was chosen so that the Courant number $Co = \sigma_{\max}\delta t/\delta x$ was approximately equal to 2. Results of the finite difference calculations are shown at time $t = 0.25$.

One of the distinctive features of the solution is the presence of a contact discontinuity (transitional wave) of large amplitude, related to the formation of a solvent bank. It is apparent from the figure that the finite difference solutions with 100 and 500 gridblocks are unable to resolve this feature. In this case, an accurate solution requires a grid with 2000 cells.

The front-tracking algorithm

Front tracking is an algorithm for constructing exact or approximate solutions to hyperbolic systems of conservation laws with general initial data (Cauchy problem):

$$\partial_t u + \partial_x f(u) = 0, \qquad u(x,0) = u_0(x). \tag{44}$$

The algorithm starts from a piecewise constant function $u_0(x)$. Each discontinuity defines a local Riemann problem, where each Riemann problem again is connected to its nearest neighbors through common constant states. All Riemann problems produce a similarity solution, called a Riemann fan, which consists of constant states separated by simple waves with finite speed of propagation. Neighboring Riemann-fans can therefore be connected through the common constant state and this way define a global solution in space, which is well-defined up to the first time two simple waves interact. If the interacting waves are discontinuities, i.e., shocks or contacts, the interaction defines a new Riemann problem. By solving the Riemann problem and inserting the corresponding local Riemann fan, the global solution can be extended in time until the next interaction and so on (see **Fig. 11**). If all simple waves are discontinuities, we can hence have an algorithm for building the global solution of the Cauchy problem.

For systems admitting continuous simple waves (rarefactions), one can similarly construct an *approximate* solution to the Cauchy problem by the above algorithm. To do so, one simply approximates each rarefaction fan by a set of constant states separated by space-time rays of discontinuity. This can be done by sampling states along the integral curve and assigning each discontinuity an appropriate wave-speed; e.g., the Rankine–Hugoniot velocity, or the eigenvalue at the left or right state. Alternatively, one can

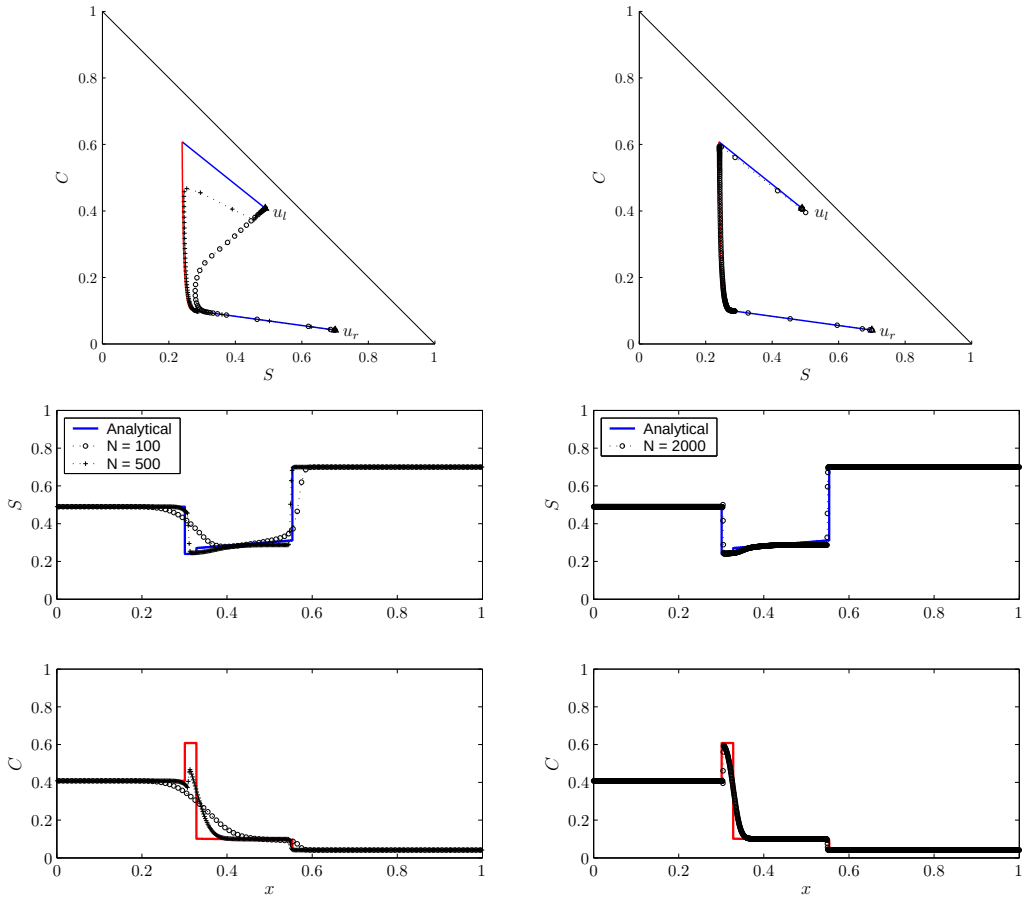

Fig. 10— Comparison between analytical and finite difference solutions for a Riemann problem of type $\mathcal{R}_3$. Left: Numerical solution with 100 and 500 gridblocks. Right: Numerical solution with 2000 gridblocks.

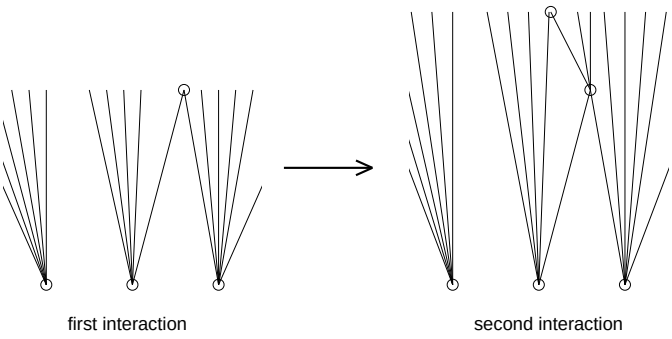

Fig. 11— Construction of a global solution by connecting local Riemann fans depicted in the (x,t)-plane.

discretize the wave speeds in the Riemann fan and then obtain the corresponding constant states.

It is also common to perform some kind of data-reduction to reduce the number of tracked discontinuities. In the current implementation, we do data-reduction on two levels. If the difference in left and right states in a Riemann problem is below a certain threshold, the Riemann fan is approximated by a single discontinuity traveling with a wave speed equal the average of the two eigenvalues of the left state. If the difference in states is even smaller, the Riemann problem is simply neglected. This data-reduction introduces a (small) error in the mass conservation that can be controlled by picking appropriate threshold values.

To sum up, the front-tracking algorithm consists of the following three key points: solution of Riemann problems, approximation of Riemann fans in terms of step functions, and tracing of discontinuities (fronts). The algorithm is usually realized in the form of a spatially-ordered list of front objects representing each discontinuity and the associated constant states and some priority queue for keeping track of colliding fronts.

Algorithm 1 The front-tracking algorithm

Construct a piecewise constant initial function $u_0(x) = u_i$
Set $\mathsf{F} = \{\emptyset\}$, $\mathsf{C} = \{\emptyset\}$, and $t = 0$
For $i = 0 : n$
  $\{\mathsf{f}_L, \ldots, \mathsf{f}_R\} = \text{RiemannSolver}(u_i, u_{i+1}, x_{i+1/2}, t)$
  $\mathsf{c} = \text{ComputeCollision}(\mathsf{F}, \mathsf{f}_L)$
  $\mathsf{C} = \text{Sort}(\{\mathsf{C}, \mathsf{c}\})$
  $\mathsf{F} = \text{InsertFronts}(\{\mathsf{F}, \{\mathsf{f}_L, \ldots, \mathsf{f}_R\})$
While $(t \le T)$ and $\mathsf{C} \neq \{\emptyset\}$ do
    $(\mathsf{c}, x_c, t_c) = \text{ExtractNextCollision}(\mathsf{C})$
    $\{\mathsf{f}_L, \ldots, \mathsf{f}_R\} = \text{ExtractCollidingFronts}(\mathsf{F}, \mathsf{c})$
    $\{\mathsf{f}_L, \ldots, \mathsf{f}_R\} = \text{RiemannSolver}(\mathsf{f}_L \to u_L, \mathsf{f}_R \to u_R, x_c, t_c)$
    $\{\mathsf{c}_L, \mathsf{c}_R\} = \text{ComputeCollision}(\mathsf{F}, \{\mathsf{f}_L, \ldots, \mathsf{f}_R\})$
    $\mathsf{C} = \text{Sort}(\{\mathsf{C}, \mathsf{c}_L, \mathsf{c}_R\})$
    $\mathsf{F} = \text{InsertFronts}(\mathsf{F}, \{\mathsf{f}_L, \ldots, \mathsf{f}_R\})$
endwhile

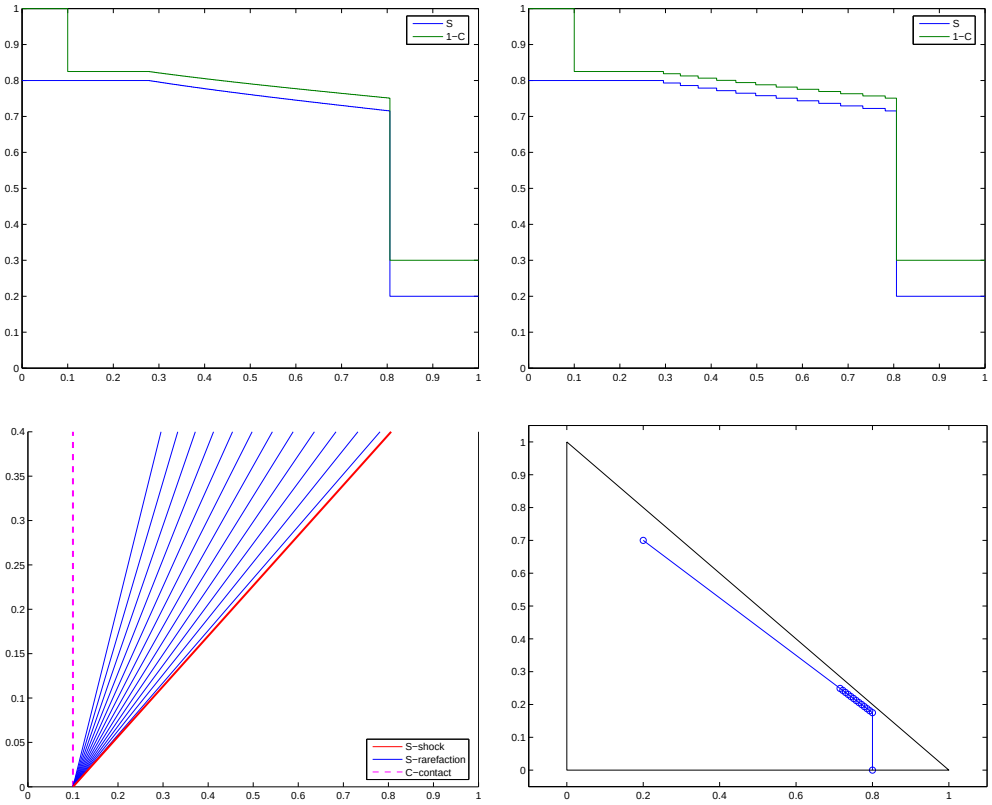

Fig. 12— (Example 1) Approximate solutions for $\delta_u = 0.001$ (upper left) and $\delta_u = 0.01$ (upper right), fronts in (x,t)-space (lower left), and solution in saturation triangle (lower right).

One-dimensional simulations

In this section we present several simple examples to demonstrate the behavior of the front-tracking algorithm. To this end, we have chosen a simple model with quadratic relative permeabilities:

$$k_{rw}(S) = \begin{cases} 0 & \text{if } S < S_{wc} = 0.2, \\ \left(\dfrac{S - S_{wc}}{1 - S_{wc}}\right)^2 & \text{otherwise,} \end{cases} \tag{45}$$

$$k_{rh}(S) = \begin{cases} 0 & \text{if } 1 - S < S_{hc} = 0.2, \\ 0.1\left(\dfrac{1 - S - S_{hc}}{1 - S_{hc}}\right) + 0.9\left(\dfrac{1 - S - S_{hc}}{1 - S_{hc}}\right)^2, \end{cases} \tag{46}$$

and viscosities given by the quarter-power rule:

$$\mu_h(\chi) = \left[\frac{1-\chi}{\mu_o^{1/4}} + \frac{\chi}{\mu_g^{1/4}}\right]^{-4}, \tag{47}$$

with

$$\mu_w = 1.0, \qquad \mu_o = 4.0, \qquad \mu_g = 0.4.$$

Example 1. The first example is a simple Riemann problem at $x = 0.1$ with left state $u_l = (0.8, 0)$ and right state $u_r = (0.2, 0.7)$. The left state lies on the border of the region of residual oil, where both eigenvalues are zero. In this case the $\mathcal{R}_2$ region covers the whole saturation triangle. The solution is therefore of the form $u_l \xrightarrow{\mathcal{C}} u_m \xrightarrow{\mathcal{S}} u_r$ and consists of a composite S-rarefaction-shock followed by a C-contact. **Fig. 12** shows approximate solutions obtained using two different tolerances for sampling the rarefactions, $\delta_u = 0.01$ and $\delta_u = 0.001$. Whereas the accuracy of the rarefaction is different, the shock and contact are represented exactly in both simulations.

Example 2. The second example is a simple Riemann problem at $x = 0.1$ with left state $u_l = (0.2, 0.7)$ and right state $u_l = (0.7, 0.2)$. The left state lies in the $\mathcal{L}$ region with $\nu_s = 0 < \nu_c = 1.25$, and the right state lies in the $\mathcal{L}_3$ region. The solution is therefore of the form $u_l \xrightarrow{\mathcal{S}} u_m^{(1)} \xrightarrow{\mathcal{C}} u_m^{(2)} \xrightarrow{\mathcal{S}} u_r$ and consists of a fast composite S-rarefaction-shock followed by a C-contact and a slow S-rarefaction. **Fig. 13** shows two approximate solutions obtained using $\delta_u = 0.01$ and $\delta_u = 0.001$.

Example 3. In this example we demonstrate the effects of data reduction. To this end, consider the unit interval $x \in [0, 1]$ with periodic boundary conditions and an initial Riemann problem with $u_l = (0.1, 0.8)$ and $u_r = (0.8, 0.1)$. We compute the solution up to time $t = 0.75$ in two ways (using $\delta_u = 0.005$):

- Using no data reduction, the simulator solved 89 full Riemann problems.
- Using data reduction when $|u_l - u_r| < 0.01$, 56 full Riemann problems were solved and 19 Riemann problems were approximated by a single wave.

Fig. 14 shows the two approximate solutions along with plots of the fronts in the (x,t) plane. We see that the data

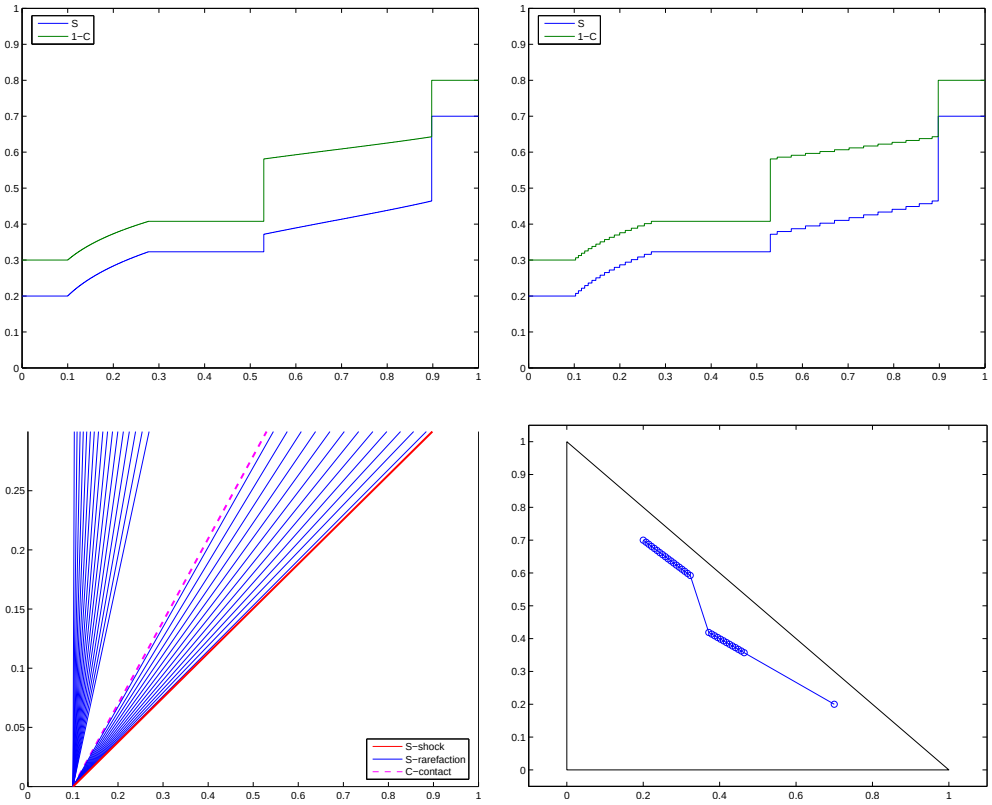

Fig. 13— (Example 2) Approximate solutions for $\delta_u = 0.001$ (upper left) and $\delta_u = 0.01$ (upper right), fronts in (x,t)-space (lower left), and solution in saturation triangle (lower right).

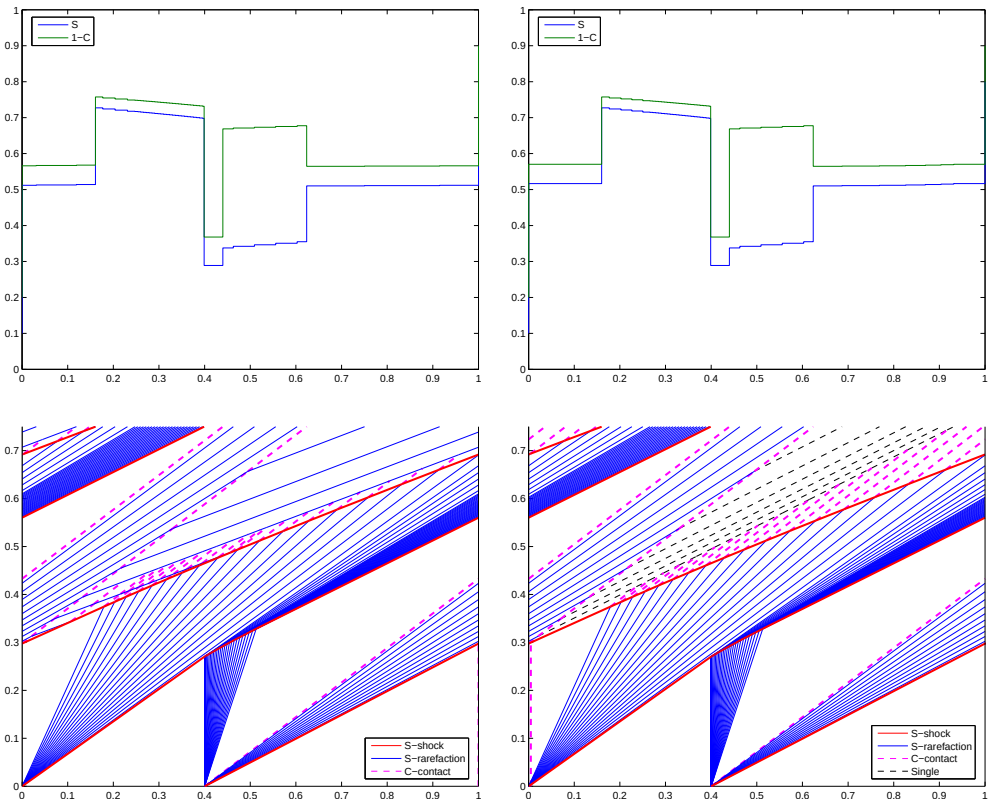

Fig. 14— (Example 3) Approximate solutions for $\delta_u = 0.005$ using no data reduction (left column) and approximating Riemann problems for which $|u_l - u_r| < 0.01$ by a single wave (right column).

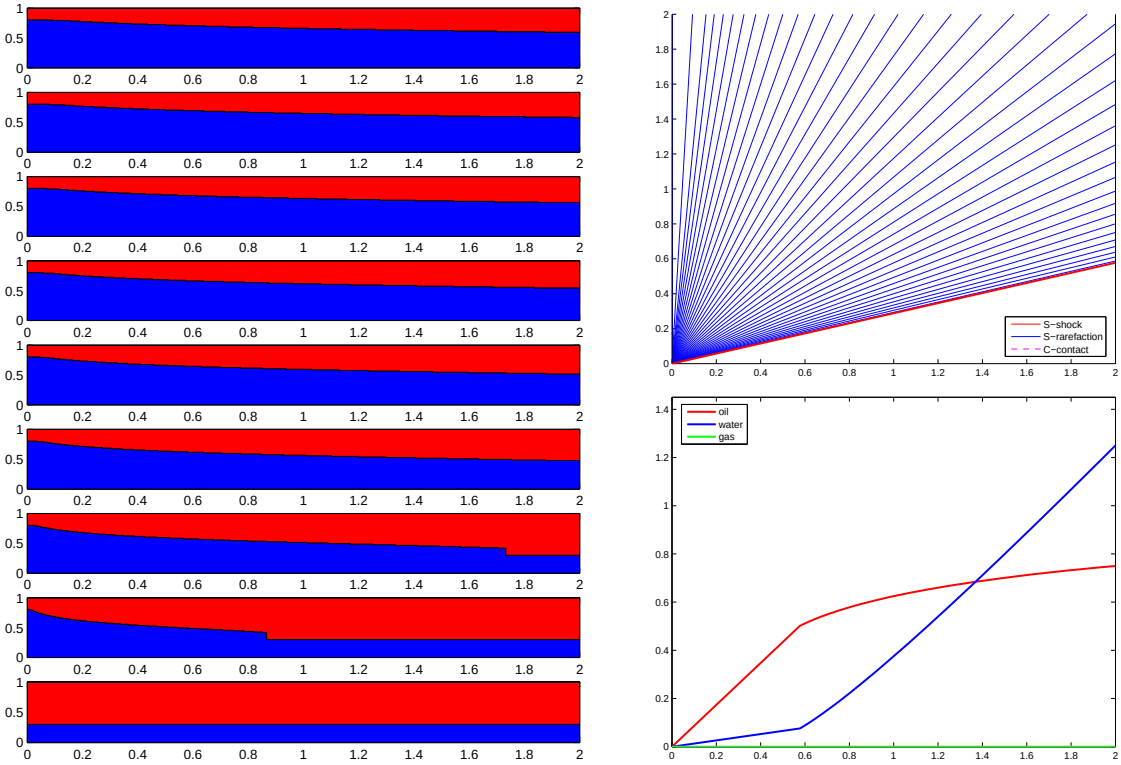

Fig. 15— (Example 4) Simulation of water injection. Left column: plot of fluid composition in reservoir at times $t = 0 : 0.25 : 2.0$ from bottom to top. Right column: fronts in (x, t)-plane and cumulative production curves.

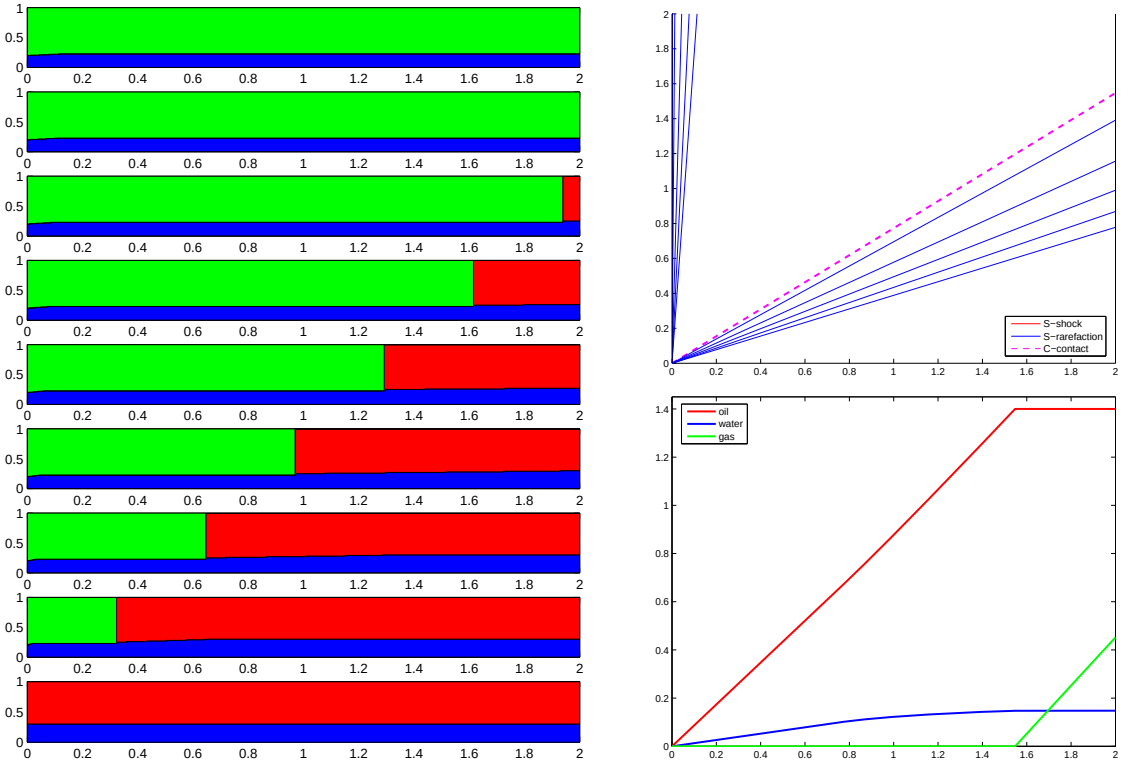

Fig. 16— (Example 4) Simulation of solvent injection. Left column: plot of fluid composition in reservoir at times $t = 0 : 0.25 : 2.0$ from bottom to top. Right column: fronts in (x, t)-plane and cumulative production curves.

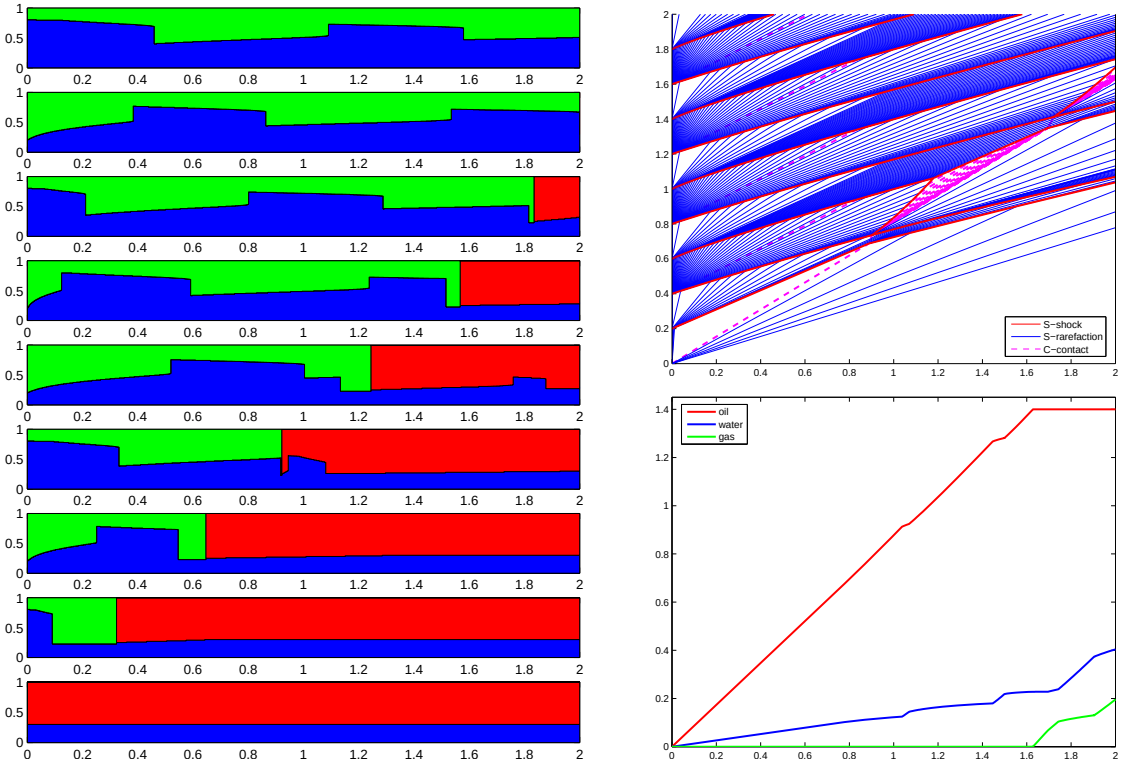

Fig. 17— (Example 4) Simulation of alternating water and solvent injection. Left column: plot of fluid composition in reservoir at times $t = 0 : 0.25 : 2.0$ from bottom to top. Right column: fronts in (x, t)-plane and cumulative production curves.

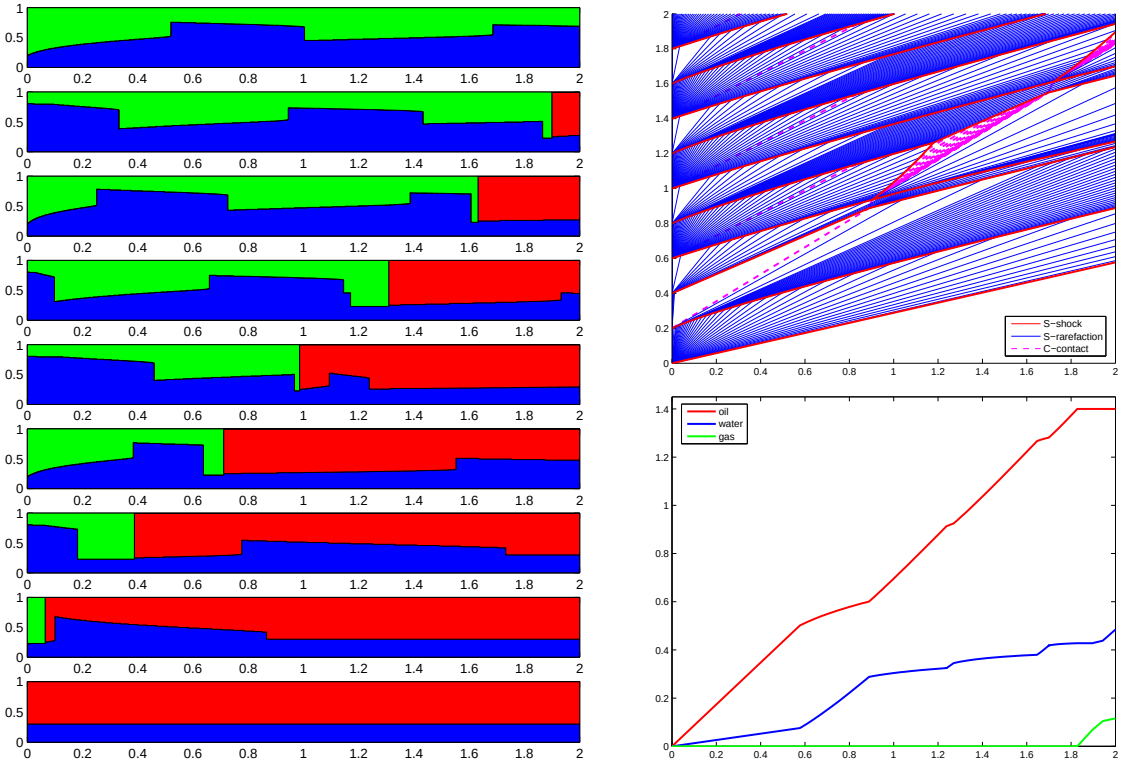

Fig. 18— (Example 4) Simulation of alternating solvent and water injection. Left column: plot of fluid composition in reservoir at times $t = 0 : 0.25 : 2.0$ from bottom to top. Right column: fronts in (x, t)-plane and cumulative production curves.

reduction has been applied to two different sorts of interactions: interaction of a S-rarefaction and the C-contact emanating from $(0, 0.3)$; and interaction of these data-reduced waves and the secondary waves produced by the interaction of the S-rarefaction emanating from $(0, 0)$ with the fast S-shock emanating from $(0, 0.3)$. The data reduction had little effect on the accuracy since the two approximate solutions are virtually indistinguishable.

Example 4. Consider now a reservoir $x \in [0, 2]$ initially filled with a fluid of composition $(0.3, 0)$. To produce the reservoir four different strategies were proposed:

1. Continuous water injection.
2. Continuous solvent (gas) injection.
3. Alternating solvent and water, with periods $\Delta t = 0.2$.
4. Alternating water and solvent, with periods $\Delta t = 0.2$.

(The trained reservoir engineer will of course immediately see that the second strategy is best, but we consider all four to illustrate the performance of the front-tracking method).

Simulations of the four strategies are shown in **Fig. 15** to **Fig. 18**. The simulation of each of the two first strategies involved one Riemann solution and wave interactions only at the outflow boundary, whereas the simulation of each of the WAG strategies involved about 1700 wave interactions and 450 Riemann solutions.

Streamline Simulations

The front-tracking method can be used as part of a streamline solver to simulate multidimensional miscible gas displacements. The streamline solver uses a sequential splitting method, in which each saturation step typically involves several thousand streamlines, resulting in a very large number of calls to the Riemann solver. A key point in obtaining an efficient solver is therefore to use the data-reduction algorithm illustrated in Example 3 to reduce the number of calls to the Riemann solver.

Example. We consider a three-dimensional rectangular reservoir model consisting of a subsample ($30 \times 110 \times 15$ gridblocks) of the highly heterogeneous shallow-marine Tarbert formation from the 10th SPE comparative solution project.[32] The permeability varies six orders of magnitude in the horizontal and ten orders of magnitude in the vertical direction, see **Fig. 19**. The porosity is strongly correlated to the permeability. The reservoir is initially filled with 70% oil and 30% water, $(S, C) = (0.3, 0)$, and for simplicity we neglect gravity and assume incompressible flow.

To produce the reservoir, we introduce a five-spot well configuration with one vertical injection well in the center and four vertical producers at the corners, and consider three different production scenarios: (i) injection of pure water, i.e., $(S, C) = (1, 0)$; (ii) injection of pure solvent, i.e., $(S, C) = (0, 1)$; and (iii) a WAG cycle where the injected fluid composition is changed between pure water and pure solvent every 200 days, starting at day 400. **Fig. 20** shows

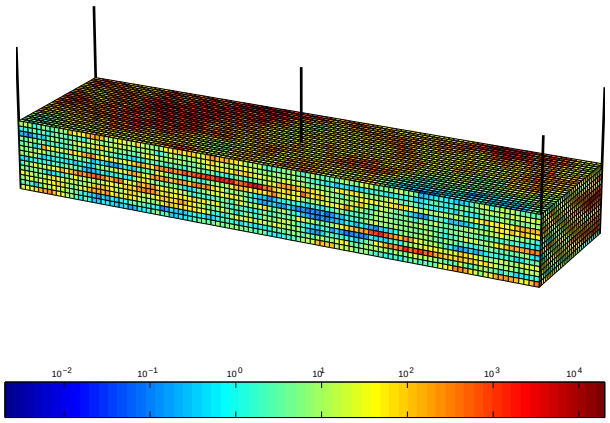

Fig. 19— Logarithm of horizontal permeability and well configuration for the Tarbert formation.

a comparison of production curves for 2000 days of production with the three scenarios. From these results, one can conclude that the recovery efficiency of the WAG scheme is higher than that of either water injection and gas injection alone, even though no attempt was made to optimize the WAG ratio or slug size.

Conclusions

In this paper we have presented an efficient computational framework for the simulation of first-contact miscible gas injection processes. The framework is based on three key technologies: (1) a streamline method that decouples the three-dimensional transport equations into a set of one-dimensional problems along streamlines; (2) a front-tracking algorithm for the accurate (or even exact) solution of general one-dimensional initial and boundary-value problems; and (3) an analytical Riemann solver for the first-contact miscible system, used as a building block in the front-tracking method.

Under certain simplifying assumptions, the system describing two-phase, three-component, first-contact miscible flow is a 2×2 hyperbolic system. It is not, however, strictly hyperbolic. Using an analogy with the system of equations governing polymer flooding,[11,12] we give the complete solution to the Riemann problem. We show that the solution may involve more than two waves, one of which is always a contact discontinuity.

The computational efficiency of the front-tracking method relies heavily on the availability of an analytical Riemann solver, and the use of a proper data-reduction algorithm to approximate (or even discard) Riemann problems of small amplitude. The solvent system studied here has two features that make the front-tracking scheme particularly attractive: (1) rarefaction curves and shock curves coincide in composition space, so there is no need to perform (an expensive) numerical integration to characterize rarefaction waves; (2) some waves are contact discontinuities, which are not self-sharpening. Such waves are very sensitive to numerical diffusion introduced by classical finite difference schemes, but they are resolved *exactly* in a front-tracking solution.

The integration of analytical Riemann solvers, the front-tracking method, and streamline tracing, offers the poten-

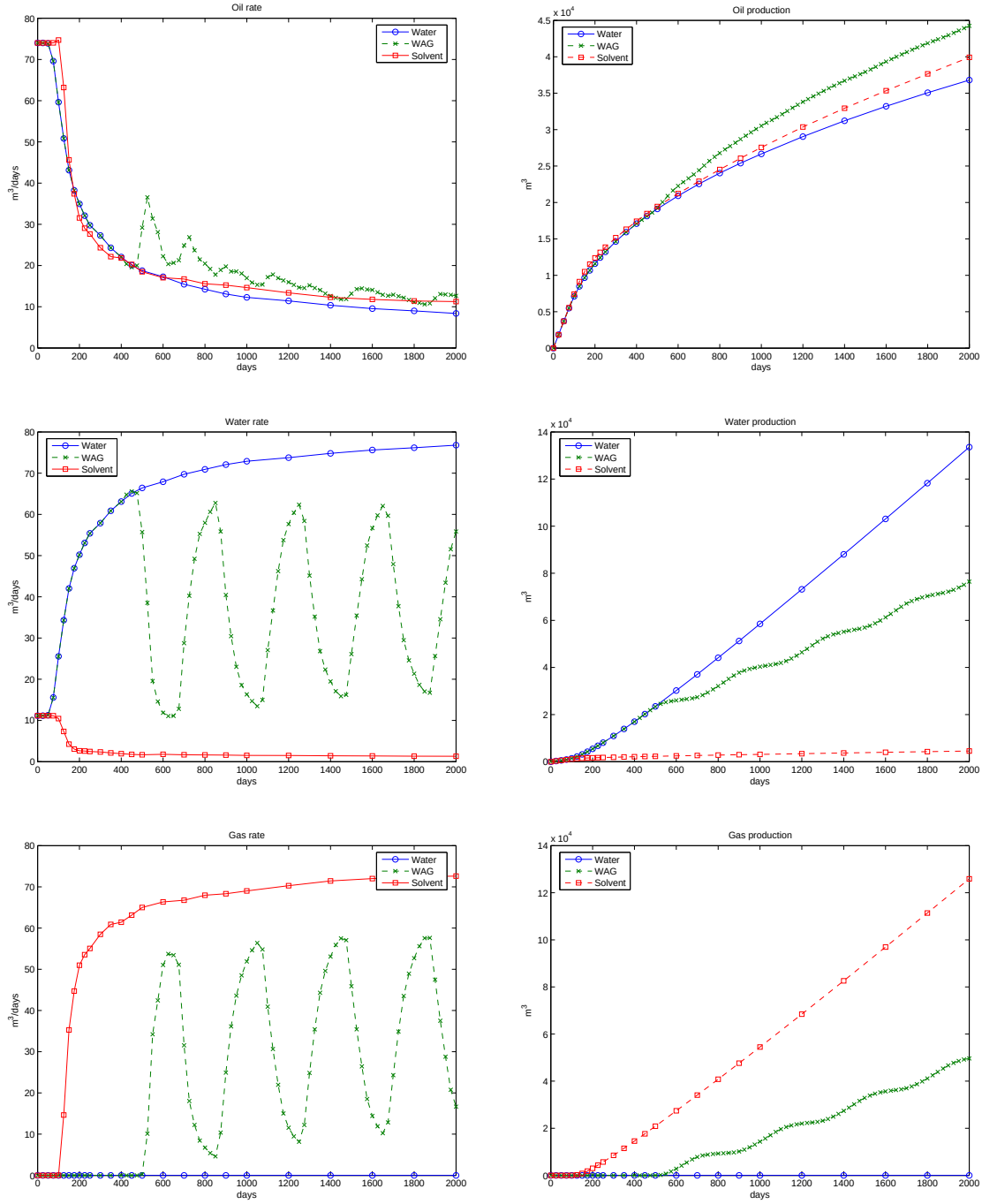

Fig. 20— Rates and cumulative production curves for water, solvent and WAG injection for a subsample of the SPE10 reservoir model.

tial for fast and accurate prediction of miscible gas and WAG injection in real reservoirs. In the paper, several representative examples are used to illustrate the excellent behavior of the front-tracking method. In particular, we present an application of this computational framework for the simulation of miscible flooding in a three-dimensional, highly heterogeneous formation, and demonstrate that a miscible water-alternating-gas injection scheme is more efficient than waterflooding or gas injection alone. Although this was not pursued here, this fast computational tool could have been used in an optimization loop for designing optimal WAG schemes (e.g., WAG ratio and slug size).

The work presented here can be extended in a number of ways. An important extension is to account for viscous fingering. Empirical models have been devised that replace the effective solvent flux in such a way that the dispersive effect of viscous fingering is captured.[33,34] Analytical solutions to particular cases have been developed by Blunt and Christie.[35] A miscible model that accounts for trapped and dendritic oil has been analyzed by O'Steen and Huang.[36] An interesting but challenging extension would be to consider multicontact miscible problems, in which the hydrocarbon components do *not* mix in all proportions. Analytical solutions for particular initial and injection states have been presented recently by LaForce and Johns.[37] Other physical processes, such as gravity, capillarity, and compressibility, may also be incorporated into the streamline simulator.

Nomenclature

Roman letters

A	Jacobian matrix of the system, dimensionless
C	solvent concentration, dimensionless
$\mathcal{C}$	Wave of the C-family
f	flux vector, dimensionless
f	water fractional flow, dimensionless
f_α	fractional flow of the α-phase, dimensionless
F_i	mass flux of the i-component, m/L^{2}t
k	absolute permeability, L^2
$k_{r\alpha}$	relative permeability of the α-phase, dimensionless
$\mathcal{L}$	left region of ternary diagram with $\nu_s < \nu_c$
m_i	mass of the i-component p.u. bulk volume, m/L^3
p	global pressure, m/Lt^2
r_i	eigenvector of the i-family, dimensionless
$\mathcal{R}$	right region of ternary diagram with $\nu_s > \nu_c$
S	water saturation, dimensionless
S_α	saturation of the α-phase, dimensionless
$S_{\alpha c}$	immobile saturation of the α-phase, dimensionless
$\mathcal{S}$	Wave of the S-family
t	time, t
$\mathcal{T}$	transition curve
u	solution vector, dimensionless
U	self-similar solution vector, dimensionless
$\mathcal{U}$	unit triangle or ternary diagram
v_T	total velocity, L/t
v_α	velocity of the α-phase, L/t
V_s	convexity function of the S-family
$\mathcal{W}_i$	wave of the i-family
x	space coordinate, L

Greek letters

δ_u	tolerance for rarefaction sampling, dimensionless
ζ	self-similarity variable, dimensionless
λ_T	total mobility, Lt/m
λ_α	relative mobility of the α-phase, Lt/m
μ_α	dynamic viscosity of the α-phase, m/Lt
ν_i	eigenvalue of the i-family, dimensionless
ρ_α	density of the α-phase, m/L^3
σ	speed of a traveling shock, dimensionless
ϕ	porosity, dimensionless
χ	solvent mass fraction, dimensionless
χ_i	mass fraction of the i-component, dimensionless

Subscripts

c	C-characteristic family
g	gas component
h	hydrocarbon phase
l	left state
m	intermediate constant state
o	oil component
r	right state
s	S-characteristic family
w	water component or aqueous phase

Acknowledgements

R.J. gratefully acknowledges financial support from the industrial affiliates of the Stanford University Petroleum Research Institute for Numerical Simulation (SUPRI-B) and Gas Injection (SUPRI-C). K.-A.L. gratefully acknowledges financial support from the Research Council of Norway under grant number 158908/I30.

References

[1] F. I. Stalkup Jr. *Miscible Displacement*, volume 8 of *SPE Monograph Series*. Society of Petroleum Engineers, Dallas, TX, 1983.

[2] L. W. Lake. *Enhanced Oil Recovery*. Prentice-Hall, Englewood Cliffs, NJ, 1989.

[3] F. M. Orr Jr. *Theory of Gas Injection Processes*. Stanford University, 2002.

[4] G. A. Pope. The application of fractional flow theory to enhanced oil recovery. *Soc. Pet. Eng. J.*, 20(3):191–205, June 1980. *Petrol. Trans.* AIME, 269.

[5] F. G. Helfferich. Theory of multicomponent, multiphase displacement in porous media. *Soc. Pet. Eng. J.*, 21(1):51–62, February 1981. *Petrol. Trans.* AIME, 271.

[6] G. J. Hirasaki. Application of the theory of multicomponent, multiphase displacement to three-component, two-phase surfactant flooding. *Soc. Pet. Eng. J.*, 21(2):191–204, April 1981. *Petrol. Trans.* AIME, 271.

[7] Y. Wang and F. M. Orr Jr. Analytical calculation of the minimum miscibility pressure. *Fluid Phase Equilib.*, 139:101–124, 1997.

[8] K. Jessen, M. L. Michelsen, and E. H. Stenby. Global approach for calculation of the minimum miscibility pressure. *Fluid Phase Equilib.*, 153:251–263, 1998.

[9] K.-A. Lie and R. Juanes. A front-tracking method for the simulation of three-phase flow in porous media. *Comput. Geosci.*, 2004. (In review).

[10] R. Juanes, K.-A. Lie, and V. Kippe. A front-tracking method for hyperbolic three-phase models. In *European Conference on the Mathematics of Oil Recovery, ECMOR IX*, volume 2, paper B025, Cannes, France, August 30–September 2 2004.

[11] E. L. Isaacson. Global solution of a Riemann problem for a non-strictly hyperbolic system of conservation laws arising in enhanced oil recovery. Technical report, The Rockefeller University, New York, 1980.

[12] T. Johansen and R. Winther. The solution of the Riemann problem for a hyperbolic system of conservation laws modeling polymer flooding. *SIAM J. Math. Anal.*, 19(3):541–566, 1988.

[13] T. Johansen and R. Winther. The Riemann problem for multicomponent polymer flooding. *SIAM J. Math. Anal.*, 20(4):908–929, 1989.

[14] T. Johansen, A. Tveito, and R. Winther. A Riemann solver for a two-phase multicomponent process. *SIAM J. Sci. Comput.*, 10(5):846–879, 1989.

[15] H. Holden and N. H. Risebro. *Front Tracking for Hyperbolic Conservation Laws*. Springer, New York, 2002.

[16] N. H. Risebro. A front-tracking alternative to the random choice method. *Proc. Amer. Math. Soc*, 117(4):1125–1129, 1993.

[17] A. Bressan and P. LeFloch. Uniqueness of weak solutions to systems of conservation laws. *Arch. Rational Mech. Anal.*, 140(4):301–317, 1997.

[18] I.-L. Chern, J. Glimm, O. McBryan, B. Plohr, and S. Yaniv. Front tracking for gas dynamics. *J. Comput. Phys.*, 62:83–110, 1986.

[19] J. Glimm, B. Lindquist, O. McBryan, and L. Padmanabhan. A front tracking reservoir simulator, five-spot validation studies and the water-coning problem. In R. E. Ewing, editor, *Mathematics of Reservoir Simulation*, volume 1 of *Frontiers in Applied Mathematics*. SIAM, 1983.

[20] N. H. Risebro and A. Tveito. Front tracking applied to a nonstrictly hyperbolic system of conservation laws. *SIAM J. Sci. Stat. Comput.*, 12(6):1401–1419, 1991.

[21] M. J. King and A. Datta-Gupta. Streamline simulation: A current perspective. *In Situ*, 22(1):91–140, 1998.

[22] V. Haugse, K. H. Karlsen, K.-A. Lie, and J. R. Natvig. Numerical solution of the polymer system by front tracking. *Transp. Porous Media*, 44:63–83, 2001.

[23] E. Zauderer. *Partial Differential Equations of Applied Mathematics*. Series in Pure and Applied Mathematics. John Wiley & Sons, New York, 1983.

[24] P. D. Lax. Hyperbolic systems of conservation laws, II. *Comm. Pure Appl. Math.*, 10:537–566, 1957.

[25] F. Ancona and A. Marson. A note on the Riemann problem for general $n \times n$ conservation laws. *J. Math. Anal. Appl.*, 260:279–293, 2001.

[26] O. A. Oleinik. Discontinuous solutions of nonlinear differential equations. *Usp. Mat. Nauk. (N.S.)*, 12:3–73, 1957. English transl. in *Amer. Math. Soc. Transl. Ser.* 2, 26:95–172.

[27] T.-P. Liu. The Riemann problem for general 2×2 conservation laws. *Trans.* Amer. Math. Soc., 199:89–112, 1974.

[28] R. Juanes. Determination of the wave structure of the three-phase flow Riemann problem. *Transp. Porous Media*, 2005. (Accepted, in press).

[29] E. Isaacson, D. Marchesin, and B. Plohr. Transitional waves for conservation laws. *SIAM J. Math. Anal.*, 21(4):837–866, 1990.

[30] S. Schecter, D. Marchesin, and B. J. Plohr. Structurally stable Riemann solutions. *J. Differential Equations*, 126:303–354, 1996.

[31] K. Jessen, E. H. Stenby, and F. M. Orr. Interplay of phase behavior and numerical dispersion in finite-difference compositional simulation. *Soc. Pet. Eng. J.*, 9(2):193–201, June 2004.

[32] M. A. Christie and M. J. Blunt. Tenth SPE comparative solution project: A comparison of upscaling techniques. *SPE Reserv. Eval. Eng.*, 4(4):308–317, 2001. url: www.spe.org/csp.

[33] E. J. Koval. A method for predicting the performance of unstable miscible displacements in heterogeneous media. *Soc. Pet. Eng. J.*, pages 145–150, June 1963. *Petrol. Trans.* AIME, 219.

[34] M. R. Todd and W. J. Longstaff. The development, testing and application of a numerical simulator for predicting miscible flood performance. *J. Pet. Technol.*, pages 874–882, July 1972.

[35] M. Blunt and M. Christie. How to predict viscous fingering in three component flow. *Transp. Porous Media*, 12:207–236, 1993.

[36] B. L. O'Steen and E. T. S. Huang. Modeling of trapped and dendritic oil mobilization during miscible displacement. *In Situ*, 14(3):285–343, 1990.

[37] T. LaForce and R. T. Johns. Analytical theory for three-phase partially miscible flow in ternary systems. In *SPE/DOE Fourteenth Symposium on Improved Oil Recovery*, Tulsa, OK, April 17–21, 2004. (SPE 89438).